Nano Research

Open Access

Research Article

Ligand engineering of Co-MOF-74 with hexaaminotriphenylene for enhanced oxygen reduction reaction in zinc-air batteries

Wei Liu, Yu Liang, Mengtian Huo, Nan Ma, Kaichi Qin, Jinfa Chang, and Zihao Xing ✉

Key Laboratory of Polyoxometalate and Reticular Material Chemistry of Ministry of Education, Faculty of Chemistry, Northeast Normal University, Changchun 130024, China

Cite this article: *Nano Research*, **2025**, *18*, 94907195. https://doi.org/10.26599/NR.2025.94907195

ABSTRACT: Zinc-air batteries hold great promise as a next-generation efficient and environmentally friendly energy technology. However, the sluggish kinetics of the oxygen reduction reaction (ORR) process pose a significant challenge to their development. To address this issue, atom dispersion catalysts are developed to maximize the utilization of metal active centers. Metal-organic frameworks (MOFs) are a series of molecular materials with high atomic-level dispersion metal utilization, but they often lack sufficient electrical conductivity. Their application in MOF electrocatalysis remains limited unless the MOF material is transferred to a carbon-based material through heat treatment. To overcome this limitation, we employed coordination engineering to incorporate hexaaminotriphenylene (HATP) molecules with strong conjugation into Co-MOF-74. The resulting Co-MOF-74-HATP catalyst represents high activity, achieving an ORR half-wave potential ($E_{1/2}$) of 0.84 V and demonstrating good stability ($\Delta E_{1/2}$ = 20 mV after 10,000 cycles). Additionally, the Co-MOF-74-HATP also performs a 320 mV overpotential (10 mA·cm^{-2}) for the oxygen evolution reaction. Meanwhile, Co-MOF-74-HATP displays a peak power density of 96.6 mW·cm^{-2} in zinc-air batteries, surpassing the commercially available Pt/C + RuO_2. This work presents a new pathway to design MOF-based ORR catalysts and provides a new direction for the preparation of key materials for zinc-air battery (ZAB).

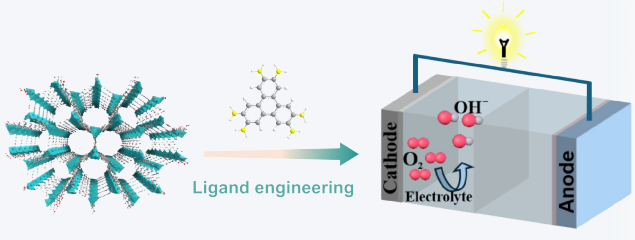

KEYWORDS: molecular catalysts, oxygen reduction reaction, zinc-air battery, coordination environment, metal-organic framework

1 Introduction

Metal-air batteries are environmentally friendly and highly efficient energy conversion devices which occupy an important position in future sustainable energy [1–7]. However, the oxygen reduction reaction (ORR) in the air cathode involves more electron reactions and requires a larger overpotential to overcome a larger energy barrier, thus affecting the overall energy conversion efficiency [8–11]. In order to improve the energy conversion, it is more important to rational design catalysts to achieve efficiency and durability. At present, platinum (Pt)-based catalysts are the most commonly utilized in ORR processes [5, 6]. The expensive cost and the limited resource supply force researchers to search for non-Pt-based ORR catalysts with high efficiency [12–15]. In transition metal catalysts, the atomic-dispersion active sites of M–N_x (M: transition metal) and M–O_x structures show high electrocatalytic activity in the ORR reaction [16–24]. The synthesized M–N_x and M–O_x structures are often pyrolyzed at high temperatures, easily forming an uncontrolled inhomogeneous coordination environment [25]. Thus, complicating the research of the relationships between structure and performance [26]. Therefore, developing catalysts with well-defined active sites is an important challenge.

To study atomically dispersed M–N_x and M–O_x structures while avoiding damage to the overall structure under high-temperature conditions, metal-organic frameworks (MOFs), which have a large surface area and tunable pore structure, could construct the M–O_x structures with definite active sites at the atomic-dispersion level. This makes MOFs as a catalytic-mechanism model system attract great attention from researchers [27–31]. MOFs molecular catalysts can utilize the special porous-mesh structure at the molecular level to improve the reaction rate of the catalyst. In this regard, Raymond Jasinski firstly discovered the Co-phthalocyanine could show ORR activity [32]. Since then, MOF molecular catalysts have been favored by researchers and have become a promising new star in the catalysis field because of their unique structure and good

Received: October 25, 2024; **Revised:** November 24, 2024
Accepted: December 16, 2024

✉Address correspondence to xingzh612@nenu.edu.cn

catalytic activity with a higher metal-active-site density. However, MOF-based catalysts have some universal problems, such as the poor electrical conductivity of the active sites, which is due to the limited overlap between the π orbital and the d orbital of the metal ion [33]. To solve these problems, MOFs could be designed by adjusting the conjugation-ligand linkers. For example, Magdalena Ola Cichocka et al. added metal porphyrins to Zr-MOF to improve the electron transport capacity in MOF [34, 35]. This strategy can significantly enhance the conductivity of catalytic active centers. Therefore, when designing ORR-MOF materials, it is crucial for researchers to investigate the mechanism by which conjugated-ligand linkers promote ORR activity at active centers in MOF molecular catalysts.

Based on this understanding, in this work, we successfully coordinated hexaaminotriphenylene (HATP) with the large π-conjugated groups into the Co active metal sites within Co-MOF-74. According to the spectroscopy results, the ligand effect and electronic interactions of HATP altered the electronic conductivity and surface valence state of Co, resulting in good catalytic activity with an ORR half-wave potential ($E_{1/2}$) of 0.84 V vs. reversible hydrogen electrode (RHE). Meantime, Co-MOF-74-HATP only needs an overpotential of 320 mV (10 mA·cm^{-2}) for oxygen evolution reaction (OER), which is much lower than that of to RuO_2. When the ZAB was assembled using Co-MOF-74-HATP as the air electrode, the peak power density achieved was measured at 96.6 mW·cm^{-2}. It could be illustrated that the high ORR performance of Co-MOF-74-HATP makes it a competitive catalyst among MOF molecular catalysts for practical applications in ZABs. This work is helpful to rationally design MOF-based molecular catalysts for high-performance oxygen reduction reactions in the future and gain a clear insight into their structure–activity relationships.

2 Experimental

2.1 Materials and synthesis

2.1.1 Chemicals

$Co(NO_3)_2·6H_2O$, 2,5-dihydroxyterephthalic acid (H_4DOBDC), KOH, commercial Pt/C, and RuO_2 were procured from Aladdin Industrial Corporation. HATP was purchased from Jilin Zhongke Research Arsenic Technology Co., Ltd. N,N-Dimethylformamide (DMF) and anhydrous ethanol were sourced from Beijing Reagent Factory. Ultrapure water was utilized in all experimental procedures.

2.1.2 Synthesis of Co-MOF-74

$Co(NO_3)_2·6H_2O$ and H_4DOBDC were added in 90 mL ethanol–DMF–water. After being mixed evenly, the mixture was heated at 100 °C for 1 day. Then, the product was washed with water and ethanol. After drying the product in a vacuum oven (the condition is 80 °C for 1 day), the target Co-MOF-74 was obtained and was ready for subsequent use.

2.1.3 Synthesis of Co-MOF-74-HATP

20 mg of above-mentioned Co-MOF-74 and 10 mg of HATP were incorporated into 1 mL of methanol solution and then ultrasonic treatment for 10 min. Then, the mixture was heated at 70 °C for 3 h to obtain the synthetic product Co-MOF-74-HATP.

3 Results and discussion

Figure 1(a) illustrates the scheme of ligand engineering with HATP in the Co-MOF as prepared. The synthesis of Co-MOF was accomplished through solvothermal method using cobaltous nitrate hexahydrate and 2,5-dihydroxyterefenic acid. Then, the self-assembly method was utilized by the HATP ligand with the π-conjugated large skeleton in Co-MOF-74-HATP (see the experimental section for details). It is interesting that the color of the Co-MOF-74 powder performs from yellow to black after the addition of HATP ligand, which proves the coordination effect of the HATP ligand (the color is different from that of the physically mixed Co-MOF-74 and HATP) (Fig. S1 in the Electronic Supplementary Material (ESM)). Meanwhile, the morphology of Co-MOF-74 still maintains the hexagonal prism shape in scanning electron microscopy (SEM) and transmission electron microscopy (TEM) images (Figs. S2 and S3 in the ESM and Figs. 1(b)–1(d)), but the surface becomes rough after the addition of HATP ligand. The energy dispersive spectroscopy (EDS) mapping of the as-formed compound shows that the elements of C, N, O, and Co are well-distributed in Fig. 1(e) and Fig. S4 in the ESM. Therefore, it can be surmised that HATP and Co-MOF-74 are self-assembled by the ligand effect, which is named Co-MOF-74-HATP. Meanwhile, the results of the inductively coupled plasma-atomic emission spectroscopy (ICP-AES) analysis showed that the Co content was 14.28 wt.% (Co-MOF-74) and 11.13 wt.% (Co-MOF-74-HATP), respectively.

To elucidate the linkage structure of Co-MOF-74-HATP, X-ray diffraction (XRD) analysis demonstrates that three distinct diffraction peaks at 6.8°, 11.8° and 25.7° are associated with the crystal planes of (110), (300), and (511), which was matching the simulated Co-MOF-74 (Fig. 1(f)) [36, 37]. As a result of the addition of the HATP ligand, the Co-MOF-74-HATP still maintains the Co-MOF-74 crystal structure, but there is a slight shift from 6.8° and 11.8° to 6.7° and 11.7°. The expansion of the (110) and (300) Co-MOF lattice skeletons may be caused by HATP entering the channels of Co-MOF-74 (Fig. S5 in the ESM) [33]. When HATP entered the channels of Co-MOF-74, the pore volume decreased dramatically from 784.35 m^2·g^{-1} to 25.71 m^2·g^{-1} by the nitrogen (N) adsorption/desorption isotherm plots, which also confirms that HATP has entered the pores of Co-MOF-74 (Fig. S6 in the ESM) [38, 39].

The changes in functional groups could be characterized by Fourier transform infrared spectroscopy (FTIR) and Raman spectra in Fig. 1(g) and Fig. S7 in the ESM. In the FTIR spectrum of Co-MOF-74, the infrared broad peak of 3418 cm^{-1} is identified to the O–H stretching vibration, which was the molecular possessing a small amount of water. The peaks at 1556 and 1409 cm^{-1} correspond to the symmetric and antisymmetric stretching vibrations associated with the carboxylate ion (COO^-). The peak at 1240 cm^{-1} was associated with the stretching vibration of the C–O bond. The corresponding peaks at 884 and 815 cm^{-1} were ascribed to the out-of-plane bending vibrations of the C=C–H bond in the benzene ring [40]. The peak at 586 cm^{-1} was the vibrational mode of the Co–O bond. For the infrared spectrum of HATP ligands, the absorption peaks at 3338 and 3228 cm^{-1} correspond to the asymmetric and symmetric stretching vibrations of $–NH_2$ groups on the benzene ring [19]. In Co-MOF-74-HATP, the stretching vibration peak of $–NH_2$ groups signal disappeared compared with that the HATP ligand, while the main functional group characteristics of Co-MOF-74 were preserved. Thus, Co-MOF-74

清华大学出版社 Tsinghua University Press | SciOpen

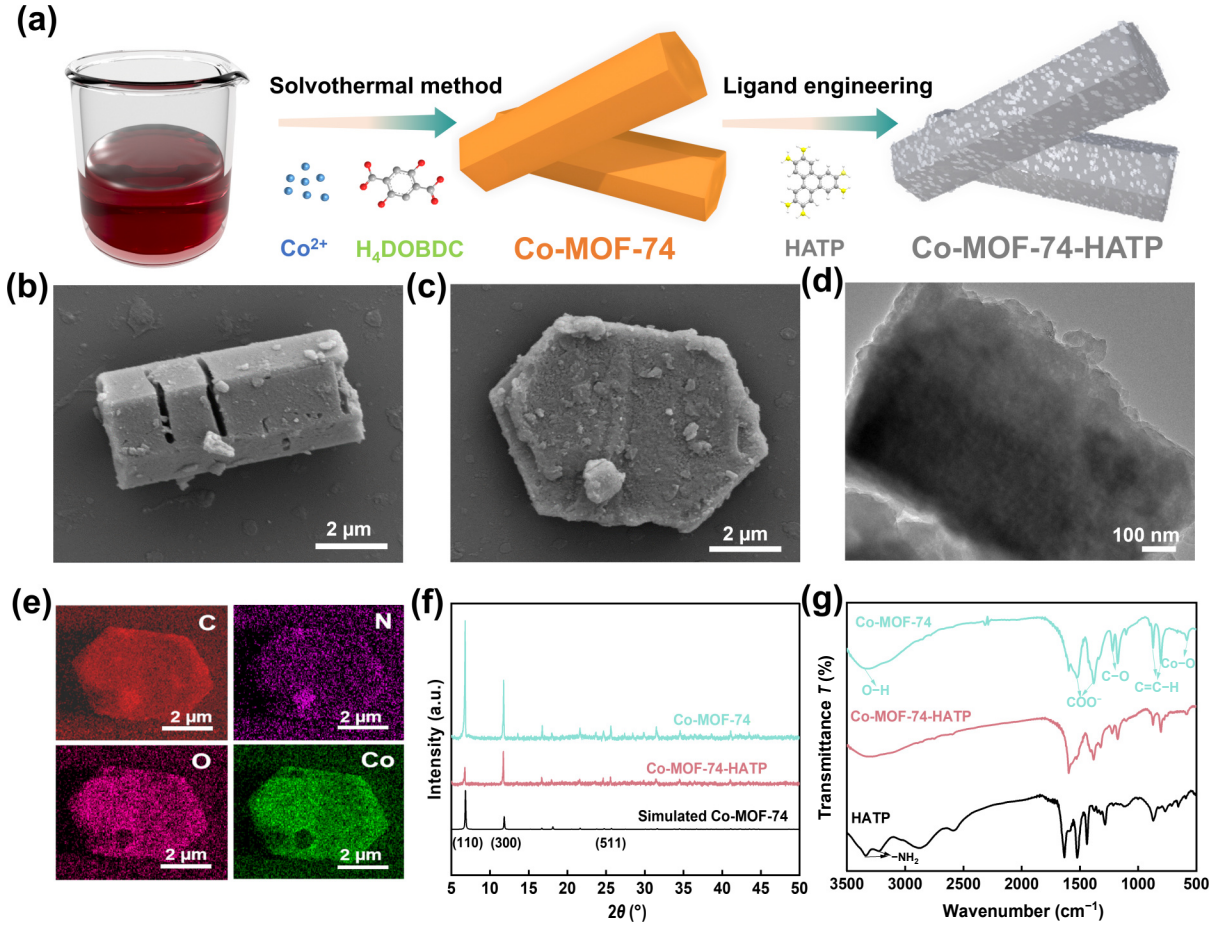

Figure 1 (a) Schematic of the two-step synthesis of Co-MOF-74-HATP. (b) and (c) SEM images of Co-MOF-74-HATP in different direction. (d) TEM image of Co-MOF-74-HATP. (e) EDS mapping elements of C (red), O (pink), N (violet) and Co (green). (f) XRD patterns of Co-MOF-74, Co-MOF-74-HATP, and the simulated Co-MOF-74. (g) FTIR spectra of Co-MOF-74, Co-MOF-74-HATP, and HATP.

and HATP were self-assembled and connected between $-NH_2$ in HATP and the Co atomic center. Meanwhile, Fig. S7 in the ESM shows the Raman spectra of Co-MOF-74, Co-MOF-74-HATP, and HATP. For Co-MOF-74, the spectral peaks at 568 and 820 cm^{-1} were the Co–O bond and the C–H bond, respectively [41]. The absorption peaks at 1278 and 1417 cm^{-1} were ascribed to the C–O vibration and the COO^- stretching vibration for the 2,5-dihydroxyterephtheric acid ligand [42]. The absorption peaks observed at 1562 and 1619 cm^{-1} were the benzene ring stretching vibration in the 2,5-dihydroxyterephthalate ligand. For HATP, the Raman peaks at 1383 and 1589 cm^{-1} were attributed to the D (defected carbon) and G (sp^2-ordered carbon) bands, respectively [19, 43]. The peak intensity ratio of the D and the G band (I_D/I_G value) of Co-MOF-74-HATP changed from 1.23 to 1.19 due to the HATP modification, indicating that after adding the HATP ligand, Co-MOF-74-HATP had an enhanced level of graphitization, which consequently led to an improvement in its conductivity.

To get insight into the differences in the chemical state and the electronic/coordination environment between Co-MOF-74 and Co-MOF-74-HATP, X-ray photoelectron spectroscopy (XPS) and X-ray absorption spectroscopy (XAS) were carried out, as shown in Fig. 2. The XPS survey spectra for the two samples identified the presence of the following elements: C 1s (285 eV), N 1s (400 eV, which was exclusively observed in Co-MOF-74-HATP), O 1s (533 eV), and Co 2p (782 eV) (Fig. 2(a)). The additional N 1s spectrum displayed two distinct peaks corresponding to C–N and Co–N at 399.4 and 400.6 eV in the Co-MOF-74-HATP (Fig. 2(b)) [41, 44]. Regarding for the changes in atomic Co, the Co 2p spectrum can be ascribed to four peaks in Co-MOF-74, the 781.5 and 797.4 eV corresponding to Co $2p_{3/2}$ and Co $2p_{1/2}$, respectively, and 785.5 and 802.2 eV were associated with satellite peaks [45, 46]. For Co-MOF-74-HATP, Co $2p_{3/2}$ shifted by 0.35 eV to higher binding energies compared to those of Co-MOF-74. This shift suggests an electron transfer from Co-MOF-74 to the HATP ligand (Fig. 2(c)) [41]. The change in the electronic environment of Co is likely due to the Co–N coordination induced by HATP.

Synchrotron XAS analysis was employed to study the coordination environment differences of Co between Co-MOF-74-HATP and Co-MOF-74. As illustrated in Fig. 2(d), the absorption edge of Co-MOF-74-HATP was positioned more closely to CoO rather than Co foil, indicating that Co in Co-MOF-74-HATP is approximately Co^{2+}. Meanwhile, the absorption edge of Co-MOF-74-HATP exhibited a shift to the high energy. As shown in Fig. S8 in the ESM, the Co valence state in Co-MOF-74-HATP was calculated to be 1.94 by the fitted oxidation states line, while a valence state of 1.78 was found for Co in Co-MOF-74. These results were consistent with the XPS results (Fig. 2(c)) and further confirmed the higher valence state of Co in Co-MOF-74-HATP than that in Co-MOF-74.

Further information about the coordination environment of Co-

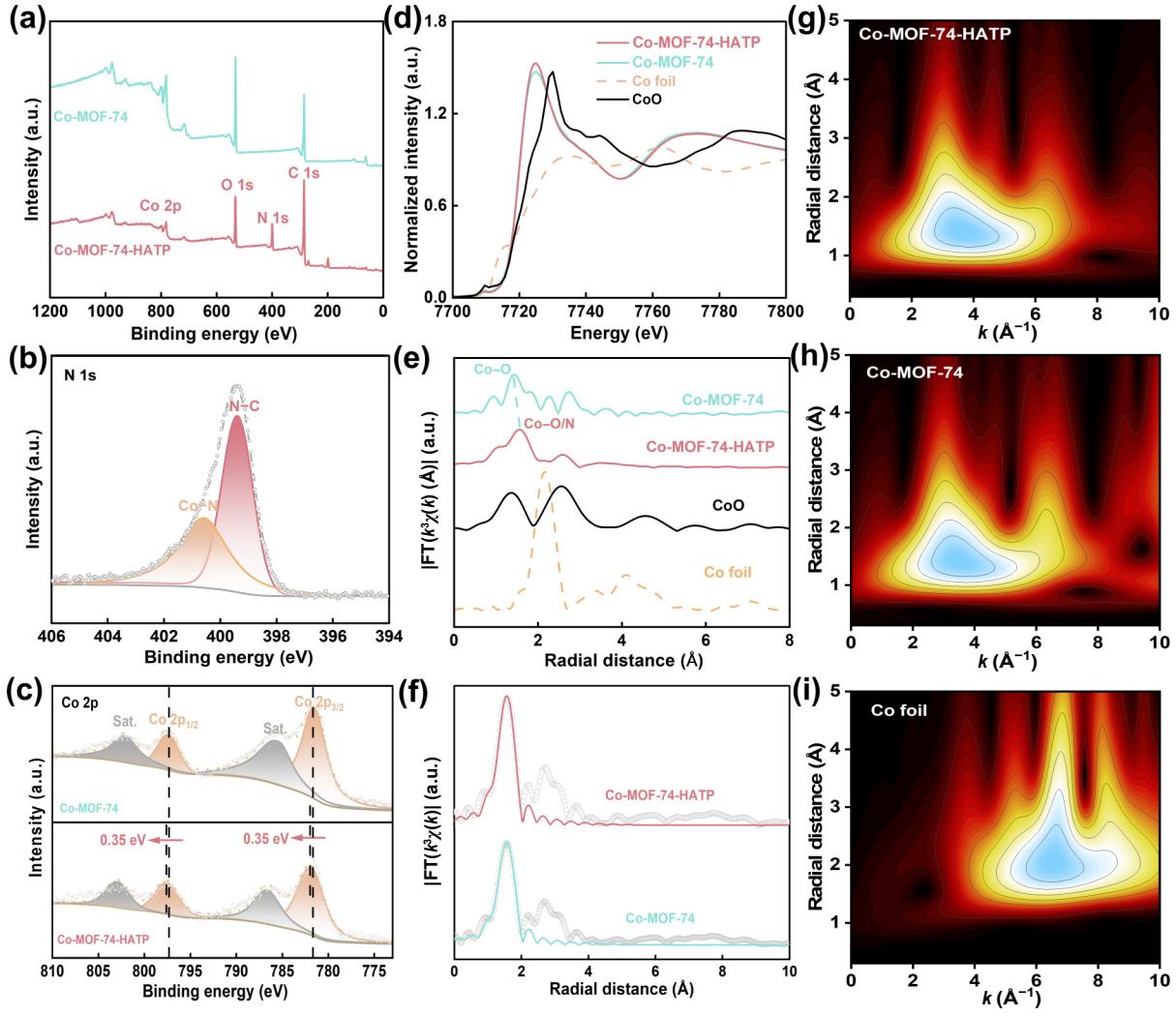

Figure 2 (a) XPS survey spectra of Co-MOF-74-HATP and Co-MOF-74. (b) XPS N 1s and (c) XPS Co 2p spectra of the samples. (d) X-ray absorption near-edge structure (XANES) spectra, and (e) EXAFS spectra of Co-MOF-74-HATP, Co-MOF-74, Co foil, and CoO. (f) Fitting of the EXAFS spectra of samples in the radial space. (g)–(i) WT of Co-MOF-74-HATP, Co-MOF-74, and Co foil.

MOF-74-HATP can be derived from the extended X-ray absorption fine structure (EXAFS) analysis, as illustrated in Fig. 2(e), Co-MOF-74 exhibited the Co–O coordination at 1.43 Å. Conversely, Co-MOF-74-HATP presented a Co–O/N coordination peak at 1.56 Å [47–50]. The Co–O/N structure for Co-MOF-74-HATP can be confirmed through fitting analysis in Fig. 2(f) and Fig. S9 in the ESM. Fitting parameters indicated that the coordination numbers of Co with O and N within the first Co coordination shell of Co-MOF-74-HATP were 5 and 1, respectively, resulting in a Co–O_5–N structure, in comparison with the Co–O_5 structure in Co-MOF-74 (Table S1 in the ESM). Wavelet transforms (WT) showed that the maximum intensities for Co-MOF-74 and Co-MOF-74-HATP could be fitted to the Co–O path and Co–O/N path at 3.5 and 3.7 Å, respectively, when compared with Co foil. This difference indicated the coordination between Co and N (Figs. 2(g)–2(i)) [47].

XAS analysis revealed distinct metal coordination environments in the two samples: Co–O_5 and Co–O_5–N configurations. We utilized the Co–O_5 configuration (Co-MOF-74) and the Co–O_5–N configuration (Co-MOF-74-HATP) to perform ORR tests [26, 51, 52]. Since HATP entered the pores of Co-MOF-74 in Co-MOF-74@HATP catalyst, carbon black (EC-300J) was added to and mixed with Co-MOF-74@HATP to promote oxygen diffusion and mass transfer during the ORR. The cyclic voltammetry (CV) curves revealed that both the Co–O_5–N and Co–O_5 configurations exhibited distinct reduction peaks in the oxygen-saturated solution, but not in the nitrogen-saturated solution, indicating the ORR catalytic activity (Fig. S10 in the ESM). Among them, the peak observed at 0.43 V could be associated with the oxidation-reduction process observed during the cyclic voltammetry of Co [53]. The limited current densities of Co-MOF-74-HATP@EC-300J under different rotation speeds, as shown in Fig. 3(a), indicated a diffusion-control process. The linear sweep voltammetry (LSV) results (Fig. 3(b)) showed that the ORR $E_{1/2}$ on Co-MOF-74-HATP@EC-300J with the Co–O_5–N configuration was 0.84 V, which was 110 mV more positive than that of on Co-MOF-74@EC-300J with the Co–O_5 configuration ($E_{1/2}$ = 0.73 V). Besides, Co-MOF-74@EC-300J with the Co–O_5–N configuration (47.82 mV·dec^{-1}) exhibited a lower Tafel slope in comparison to Co-MOF-74@EC-300J with the Co–O_5 configuration (72.71 mV·dec^{-1}), indicating a more rapid ORR kinetic process on Co-MOF-74-HATP@EC-300J (Fig. 3(c)). Moreover, the addition of HATP lowered the charge resistance in

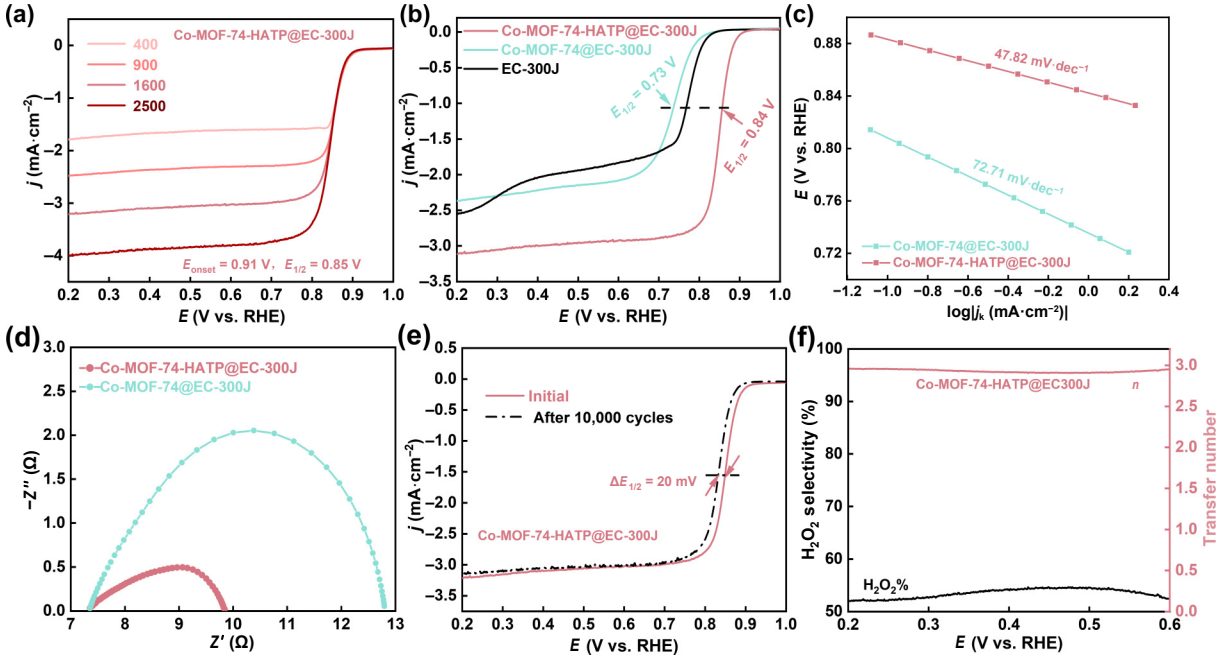

Figure 3 (a) LSV curves for Co-MOF-74-HATP@EC-300J. (b) LSV curve (1600 rpm) for Co-MOF-74,Co-MOF-74-HATP@EC-300J and EC-300J. (c) Tafel plot and (d) EIS of the samples. (e) LSV curves of Co-MOF-74-HATP@EC-300J before and after 10,000 CV cycles. (f) Electron transfer number and H_2O_2 yield for Co-MOF-74-HATP@EC-300J.

the Co–O_5–N configuration due to the significant level of graphitization of Co–O_5–N (consistent with the Raman analysis), which accelerates the ORR reaction rate (Fig. 3(d)). These results collectively indicate the Co-MOF-74-HATP is a highly efficient ORR catalyst. Additionally, an accelerated aging test of 10,000 cycles demonstrated that Co-MOF-74-HATP had excellent stability, the ORR $E_{1/2}$ only had a 20 mV negative shift compared to the initial LSV (Fig. 3(e)). After CV stability, FTIR and XRD results showed that there was no notable variation in the FTIR spectra XRD patterns before and after the CV process (Fig. S11 in the ESM). The original structure of Co-MOF-74-HATP catalyst could be maintained after the stability test. It is worth mentioning that in the research of the ORR reaction of Co–O_5–N configuration, the transferred electrons number of 2.9 which is more inclined to the $3e^-$ ORR path than in the Co–O_5 configuration (Fig. 3(f) and Figs. S12 and S13 in the ESM, consistent with the analysis of the Koutecky–Levich (K–L) plot in Fig. S12 in the ESM). Among them, the H_2O_2 yield is 53%, while the Co–O_5 structure is 75%, respectively.

Before evaluating the potential application of Co-MOF-74-HATP@EC-300J in zinc-air batteries (ZABs), an evaluation of its OER performance was conducted. Remarkably, Co-MOF-74-HATP@EC-300J exhibited overpotential of 320 mV (at 10 mA·cm^{-2}) which is notably competitive with RuO_2 (Fig. S14 in the ESM). Furthermore, Co-MOF-74-HATP@EC-300J displayed a small Tafel slope of 133 mV·dec^{-1} (Fig. S15 in the ESM) with a smaller interfacial charge-transfer resistance compared to RuO_2 in electrochemical impedance spectroscopy (EIS) (Fig. S16 in the ESM), indicating superior kinetics and charge transfer processes in OER applications. Additionally, the double-layer capacitance (C_{dl}, Figs. S17–S19 in the ESM) indicated that the electrochemical surface area (ECSA) of Co-MOF-74-HATP@EC-300J (1147.5 cm^{-2}) was more than 7.6 times that of RuO_2, indicating that Co-MOF-74-HATP is a promising candidate as air-electrode for zinc-air battery.

Thereafter, an assessment was conducted on the practical application of the Co-MOF-74-HATP@EC-300J catalyst within ZAB. An alkaline zinc-air battery was constructed using the catalyst sprayed onto carbon paper as the cathode, a zinc foil as the anode, and an electrolyte formulated from a 6 M potassium hydroxide solution combined with 0.2 M zinc acetate in Fig. 4(a). The open circuit voltage (OCV) of Co-MOF-74-HATP@EC-300J was 1.37 V, marginally higher than that of the 20% Pt/C + RuO_2 catalyst (Fig. 4(b) and Fig. S20 in the ESM). Meanwhile, Fig. 4(c) indicated that the voltage gap of Co-MOF-74-HATP@EC-300J was smaller than 20% Pt/C + RuO_2 with the increase of current density, indicating that Co-MOF-74-HATP@EC-300J has better charge–discharge performance. While the bending charge curves in Fig. 4(c) can be mainly attributed to the oxidation of the carbon paper that was used as a current collector (Fig. S21 in the ESM). Furthermore, a comparison of power densities shows that Co-MOF-74-HATP@EC-300J achieved a peak power density of 96.6 mW·cm^{-2} (Fig. 4(d)), much higher than commercial 20% Pt/C + RuO_2 electrode. Regarding the rechargeability and cycling stability (Fig. 4(e)), the ZAB with Co-MOF-74-HATP@EC-300J maintains a voltage gap of 0.77 V sustained over a duration of 500 h (1 mA·cm^{-2}). In addition, two ZABs in a series configuration could successfully power a light-emitting diode (LED) lamp (Fig. 4(f) and Fig. S22 in the ESM), emphasizing the practical applicability of Co-MOF-74-HATP.

4 Conclusions

In summary, we successfully constructed an active site in Co-MOF-74-HATP by coordinating HATP to form Co–O_5–N. Compared with Co-MOF-74, Co-MOF-74-HATP enhances the surface valence state and electrical conductivity of cobalt due to the electronic and ligand effects of HATP. Co-MOF-74-HATP exhibits high ORR catalytic activity of 0.84 V. Additionally, the Co-MOF-74-HATP demonstrates excellent OER (320 mV at 10 mA·cm^{-2}). The Co-MOF-74-HATP@EC-300J could make the zinc-air battery achieve a power density of 96.6 mW·cm^{-2} and commendable long-

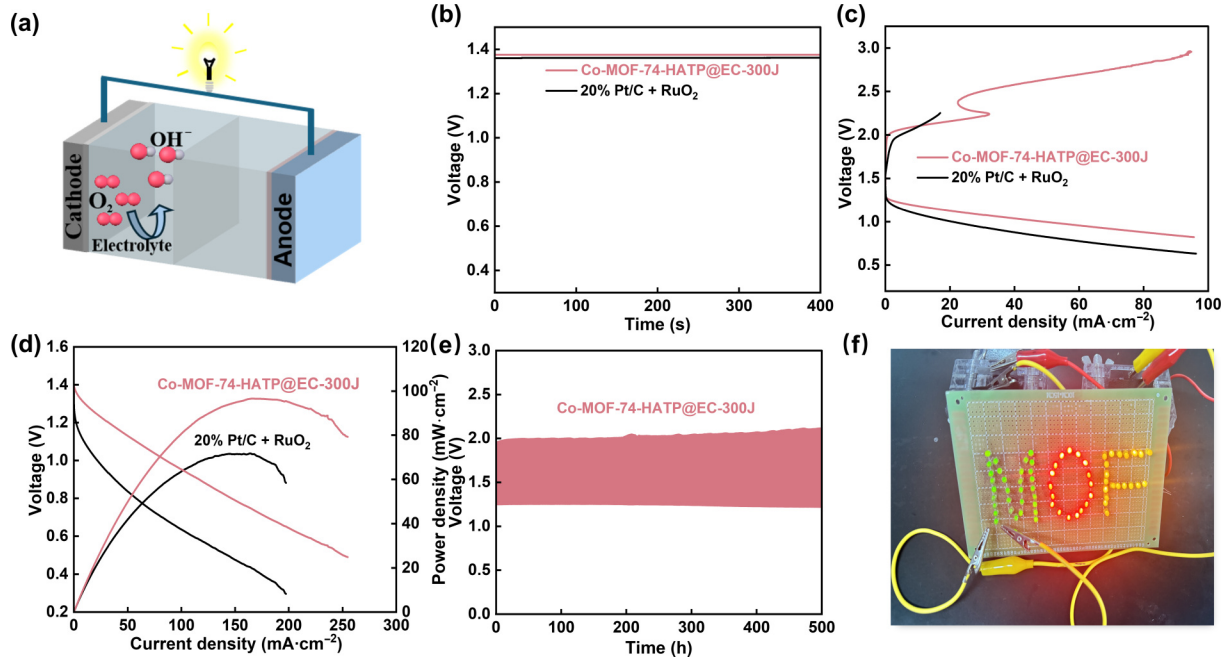

Figure 4 (a) Schematic of the assembled ZAB. (b) Open circuit voltage curve of the ZAB constructed with Co-MOF-74-HATP@EC-300J. (c) Charge and discharge curves. (d) Power density curves and (e) galvanostatic charge and discharge cycling curve at 1 mA·cm^{-2} of Co-MOF-74-HATP@EC-300J. (f) Schematic representation of two zinc-air batteries arranged in series to power LED lights.

term cycling stability. Our work offers an innovative methodology for developing molecular-based catalysts for the ORR catalyst without any heat-treatment and opens new directions for designing catalysts for zinc-air batteries.

Electronic Supplementary Material: Supplementary material (physical characterization and electrochemical properties of the catalyst test details (ORR and OER processes)) is available at https://doi.org/10.26599/NR.2025.94907195.

Data availability

All data needed to support the conclusions in the paper are presented in the manuscript and the Electronic Supplementary Material. Additional data related to this paper may be requested from the corresponding author upon request.

Acknowledgements

This work was supported by National Natural Science Foundation of China (Nos. 22202037, 22472023 and 22102105) and the Fundamental Research Funds for the Central Universities (Nos. 2412024QD014 and 2412023QD019). This work was also supported by the Science and Technology Development Plan Project of Jilin Province, China (No. 20240101192JC). We would also like to express our gratitude to the personnel at the BL17W1 beamline of the National Facility for Protein Science in Shanghai (NFPS), Shanghai Advanced Research Institute, for their assistance during the data collection process.

Declaration of competing interest

All the contributing authors report no conflict of interests in this work.

Author contribution statement

Z. H. X. and J. F. C. led the project. W. L. carried out the experiments. M. T. H. helped with the sample synthesis experiment. Y. L. and K. C. Q. participated in the drawing of the flowchart. N. M. helped complete the performance test. All authors discussed the results and provided comments. All the authors have approved the final manuscript.

Use of AI statement

None.

References

[1] Dresselhaus, M. S.; Thomas, I. L. Alternative energy technologies. *Nature* **2001**, *414*, 332–337.

[2] Whitesides, G. M.; Crabtree, G. W. Don't forget long-term fundamental research in energy. *Science* **2007**, *315*, 796–798.

[3] Cheng, F. Y.; Chen, J. Metal-air batteries: From oxygen reduction electrochemistry to cathode catalysts. *Chem. Soc. Rev.* **2012**, *41*, 2172–2192.

[4] Zhao, X.; Takao, S.; Yoshida, Y.; Kaneko, T.; Gunji, T.; Higashi, K.; Uruga, T.; Iwasawa, Y. Roles of structural defects in polycrystalline platinum nanowires for enhanced oxygen reduction activity. *Appl. Catal. B: Environ.* **2023**, *324*, 122268.

[5] Du, L.; Lv, M.; Zhang, J.; Song, H.; Dang, D.; Liu, Q.; Cui, Z.; Liao, S. Robust $InNCo_{3-x}Mn_x$ nitride-supported Pt nanoparticles as high-performance bifunctional electrocatalysts for Zn-air batteries. *ACS Appl. Energy Mater.* **2020**, *3*, 5293–5300.

[6] Tao, L.; Wang, K.; Lv, F.; Mi, H. T.; Lin, F. X.; Luo, H.; Guo, H. Y.; Zhang, Q. H.; Gu, L.; Luo, M. C. et al. Precise synthetic control of exclusive ligand effect boosts oxygen reduction catalysis. *Nat. Commun.* **2023**, *14*, 6893.

[7] Hu, L. Y.; Dai, C. L.; Chen, L. W.; Zhu, Y. H.; Hao, Y. C.; Zhang, Q. H.; Gu, L.; Feng, X.; Yuan, S.; Wang, L. et al. Metal-triazolate-framework-derived FeN_4Cl_1 single-atom catalysts with hierarchical

porosity for the oxygen reduction reaction. *Angew. Chem., Int. Ed.* **2021**, *60*, 27324–27329.

[8] Zhu, C. Z.; Li, H.; Fu, S. F.; Du, D.; Lin, Y. H. Highly efficient nonprecious metal catalysts towards oxygen reduction reaction based on three-dimensional porous carbon nanostructures. *Chem. Soc. Rev.* **2016**, *45*, 517–531.

[9] Zhao, W. Y.; Chi, B.; Liang, L. C.; Yang, P. F.; Zhang, W.; Ge, X.; Wang, L. M.; Cui, Z. M.; Liao, S. J. Optimizing the electronic structure of ordered Pt–Co–Ti ternary intermetallic catalyst to boost acidic oxygen reduction. *ACS Catal.* **2022**, *12*, 7571–7578.

[10] Lin, F. X.; Lv, F.; Zhang, Q. H.; Luo, H.; Wang, K.; Zhou, J. H.; Zhang, W. Y.; Zhang, W. S.; Wang, D. W.; Gu, L. et al. Local coordination regulation through tuning atomic-scale cavities of Pd metallene toward efficient oxygen reduction electrocatalysis. *Adv. Mater.* **2022**, *34*, 2202084.

[11] Chen, J. Y.; Li, H.; Fan, C.; Meng, Q. W.; Tang, Y. W.; Qiu, X. Y.; Fu, G. T.; Ma, T. Y. Dual single-atomic Ni-N_4 and Fe-N_4 sites constructing Janus hollow graphene for selective oxygen electrocatalysis. *Adv. Mater.* **2020**, *32*, 2003134.

[12] Yang, H.; Liu, Y. F.; Liu, X. L.; Wang, X. K.; Tian, H.; Waterhouse, G. I. N.; Kruger, P. E.; Telfer, S. G.; Ma, S. Q. Large-scale synthesis of N-doped carbon capsules supporting atomically dispersed iron for efficient oxygen reduction reaction electrocatalysis. *eScience* **2022**, *2*, 227–234.

[13] Gao, L.; Song, Y.; Xu, X. B.; Li, C.; Hu, C. Q. Mn-modified nitrogen-doped Pt-based electrocatalyst for efficient oxygen reduction in aluminum-air batteries. *Nano Res.* **2024**, *17*, 7126–7135.

[14] Xia, W.; Mahmood, A.; Liang, Z. B.; Zou, R. Q.; Guo, S. J. Earth-abundant nanomaterials for oxygen reduction. *Angew. Chem., Int. Ed.* **2016**, *55*, 2650–2676.

[15] Zhao, J. J.; Fu, C. H.; Ye, K.; Liang, Z.; Jiang, F. L.; Shen, S. Y.; Zhao, X. R.; Ma, L.; Shadike, Z.; Wang, X. M. et al. Manipulating the oxygen reduction reaction pathway on Pt-coordinated motifs. *Nat. Commun.* **2022**, *13*, 685.

[16] Miner, E. M.; Fukushima, T.; Sheberla, D.; Sun, L.; Surendranath, Y.; Dincă, M. Electrochemical oxygen reduction catalysed by Ni_3(hexaiminotriphenylene)$_2$. *Nat. Commun.* **2016**, *7*, 10942.

[17] Zhong, H. X.; Ly, K. H.; Wang, M. C.; Krupskaya, Y.; Han, X. C.; Zhang, J. C.; Zhang, J.; Kataev, V.; Büchner, B.; Weidinger, I. M. et al. A phthalocyanine-based layered two-dimensional conjugated metal-organic framework as a highly efficient electrocatalyst for the oxygen reduction reaction. *Angew. Chem., Int. Ed.* **2019**, *58*, 10677–10682.

[18] Liu, X. H.; Hu, W. L.; Jiang, W. J.; Yang, Y. W.; Niu, S.; Sun, B.; Wu, J.; Hu, J. S. Well-defined metal-O_6 in metal-catecholates as a novel active site for oxygen electroreduction. *ACS Appl. Mater. Interfaces* **2017**, *9*, 28473–28477.

[19] Lian, Y. B.; Yang, W. J.; Zhang, C. F.; Sun, H.; Deng, Z.; Xu, W. J.; Song, L.; Ouyang, Z. W.; Wang, Z. X.; Guo, J. et al. Unpaired 3d electrons on atomically dispersed cobalt centres in coordination polymers regulate both oxygen reduction reaction (ORR) activity and selectivity for use in zinc-air batteries. *Angew. Chem., Int. Ed.* **2020**, *59*, 286–294.

[20] He, Y. T.; Yang, J. B.; Wang, Y.; Jia, Y. F.; Li, H. T.; Liu, Y. N.; Liu, L. T.; Tan, Q. Atomically dispersed dual-metal ORR catalyst with hierarchical porous structure for Zn-air batteries. *ACS Appl. Mater. Interfaces* **2024**, *16*, 12398–12406.

[21] Xu, X. C.; Li, X. Y.; Lu, W. T.; Sun, X. Y.; Huang, H.; Cui, X. Q.; Li, L.; Zou, X. X.; Zheng, W. T.; Zhao, X. Collective effect in a multicomponent ensemble combining single atoms and nanoparticles for efficient and durable oxygen reduction. *Angew. Chem., Int. Ed.* **2024**, *63*, e202400765.

[22] Zhou, Y. N.; Sheng, L.; Chen, L. L.; Zhao, W. H.; Zhang, W. H.; Yang, J. L. Metal and ligand modification modulates the electrocatalytic HER, OER, and ORR activity of 2D conductive metal-organic frameworks. *Nano Res.* **2024**, *17*, 7984–7990.

[23] Liu, Y. R.; Yuan, S.; Sun, C. T.; Wang, C. L.; Liu, X. J.; Lv, Z. H.; Liu, R.; Meng, Y. Z.; Yang, W. X.; Feng, X. et al. Optimizing Fe-3d electron delocalization by asymmetric Fe–Cu diatomic configurations for efficient anion exchange membrane fuel cells. *Adv. Energy Mater.* **2023**, *13*, 2302719.

[24] Li, L. H.; Liu, X. J.; Wang, J. M.; Liu, R.; Liu, Y. R.; Wang, C. L.; Yang, W. X.; Feng, X.; Wang, B. Atomically dispersed Co in a cross-channel hierarchical carbon-based electrocatalyst for high-performance oxygen reduction in Zn–air batteries. *J. Mater. Chem. A* **2022**, *10*, 18723–18729.

[25] Jiang, K.; Ma, X. Y.; Back, S.; Zhao, J. J.; Jiang, F. L.; Qin, X. X.; Zhang, J. L.; Cai, W. B. Local coordination and reactivity of a Pt single-atom catalyst as probed by spectroelectrochemical and computational approaches. *CCS Chem.* **2021**, *3*, 241–251.

[26] Sun, K.; Dong, J. C.; Sun, H.; Wang, X. D.; Fang, J. J.; Zhuang, Z. B.; Tian, S. B.; Sun, X. M. $Co(CN)_3$ catalysts with well-defined coordination structure for the oxygen reduction reaction. *Nat. Catal* **2023**, *6*, 1164–1173.

[27] Zhao, Q.; Jiang, J. W.; Zhao, W.; Li, S. H.; Mi, W. B.; Zhang, C. Truxone-based conductive metal-organic frameworks for the oxygen reductive reaction. *J. Phys. Chem. C* **2021**, *125*, 12690–12698.

[28] Park, J.; Chen, Z. H.; Flores, R. A.; Wallnerström, G.; Kulkarni, A.; Nørskov, J. K.; Jaramillo, T. F.; Bao, Z. N. Two-dimensional conductive Ni-HAB as a catalyst for the electrochemical oxygen reduction reaction. *ACS Appl. Mater. Interfaces* **2020**, *12*, 39074–39081.

[29] Liu, X. M.; Zhuo, M. L.; Zhang, W. D.; Gao, M.; Liu, X. H.; Sun, B.; Wu, J. One-step ultrasonic synthesis of Co/Ni-catecholates for improved performance in oxygen reduction reaction. *Ultrason. Sonochem.* **2020**, *67*, 105179.

[30] Miner, E. M.; Wang, L.; Dincă, M. Modular O_2 electroreduction activity in triphenylene-based metal-organic frameworks. *Chem. Sci.* **2018**, *9*, 6286–6291.

[31] Liu, K. K.; Meng, Z.; Fang, Y.; Jiang, H. L. Conductive MOFs for electrocatalysis and electrochemical sensor. *eScience* **2023**, *3*, 100133.

[32] Jasinski, R. A new fuel cell cathode catalyst. *Nature* **1964**, *201*, 1212–1213.

[33] Talin, A. A.; Centrone, A.; Ford, A. C.; Foster, M. E.; Stavila, V.; Haney, P.; Kinney, R. A.; Szalai, V.; El Gabaly, F.; Yoon, H. P. et al. Tunable electrical conductivity in metal-organic framework thin-film devices. *Science* **2014**, *343*, 66–69.

[34] Cichocka, M. O.; Liang, Z. Z.; Feng, D. W.; Back, S.; Siahrostami, S.; Wang, X.; Samperisi, L.; Sun, Y. J.; Xu, H. Y.; Hedin, N. et al. A porphyrinic zirconium metal-organic framework for oxygen reduction reaction: Tailoring the spacing between active-sites through chain-based inorganic building units. *J. Am. Chem. Soc.* **2020**, *142*, 15386–15395.

[35] Duan, Y. X.; Wang, L. X.; Zhang, J. K.; Sun, C. Y.; Wen, R.; Dou, M. L. Surface engineering route to non-pyrolysis MOFs with high-density Co–N_x sites and 3D conductive networks for efficient oxygen reduction. *ACS Appl. Energy Mater* **2023**, *6*, 3244–3250.

[36] Albuquerque, G. H.; Fitzmorris, R. C.; Ahmadi, M.; Wannenmacher, N.; Thallapally, P. K.; McGrail, B. P.; Herman, G. S. Gas-liquid segmented flow microwave-assisted synthesis of MOF-74(Ni) under moderate pressures. *CrystEngComm* **2015**, *17*, 5502–5510.

[37] Díaz-García, M.; Sánchez-Sánchez, M. Synthesis and characterization of a new Cd-based metal-organic framework isostructural with MOF-74/CPO-27 materials. *Microporous Mesoporous Mater.* **2014**, *190*, 248–254.

[38] Gong, Y. N.; Jiao, L.; Qian, Y. Y.; Pan, C. Y.; Zheng, L. R.; Cai, X. C.; Liu, B.; Yu, S. H.; Jiang, H. L. Regulating the coordination environment of MOF-templated single-atom nickel electrocatalysts for boosting CO_2 reduction. *Angew. Chem., Int. Ed.* **2020**, *59*, 2705–2709.

[39] Angel, S. M.; Barnett, N. S.; Talin, A. A.; Foster, M. E.; Stavila, V.; Allendorf, M. D.; So, M. C. From insulator to semiconductor: Effect

of host–guest interactions on charge transport in M-MOF-74 metal-organic frameworks. *J. Mater. Chem. C* **2024**, *12*, 2699–2704.

[40] Liao, Y. X.; Li, C.; Lou, X. B.; Wang, P.; Yang, Q.; Shen, M.; Hu, B. W. Highly reversible lithium storage in cobalt 2,5-dioxido-1,4-benzenedicarboxylate metal-organic frameworks boosted by pseudocapacitance. *J. Colloid Interface Sci.* **2017**, *506*, 365–372.

[41] Jia, J. Z.; Zhao, X. H.; Hu, W. H.; Wang, Y. T.; Huang, J. F.; Huang, J. E.; Li, H.; Peng, Y.; Ma, H. Y.; Xu, C. L. Role of cobalt phthalocyanine on the formation of high-valent cobalt species revealed by *in situ* Raman spectroscopy. *J. Mater. Chem. A* **2023**, *11*, 8141–8149.

[42] Strauss, I.; Mundstock, A.; Hinrichs, D.; Himstedt, R.; Knebel, A.; Reinhardt, C.; Dorfs, D.; Caro, J. The interaction of guest molecules with Co-MOF-74: A Vis/NIR and Raman approach. *Angew. Chem., Int. Ed.* **2018**, *57*, 7434–7439.

[43] Xing, D. N.; Cui, Z. H.; Liu, Y. Y.; Wang, Z. Y.; Wang, P.; Zheng, Z. K.; Cheng, H. F.; Dai, Y.; Huang, B. B. Two-dimensional π–d conjugated metal-organic framework Fe_3(hexaiminotriphenylene)$_2$ as a photo-Fenton like catalyst for highly efficient degradation of antibiotics. *Appl. Catal. B: Environ.* **2021**, *290*, 120029.

[44] Xing, D. N.; Wang, Y. Y.; Zhou, P.; Liu, Y. Y.; Wang, Z. Y.; Wang, P.; Zheng, Z. K.; Cheng, H. F.; Dai, Y.; Huang, B. B. Co_3(hexaiminotriphenylene)$_2$: A conductive two-dimensional π–d conjugated metal-organic framework for highly efficient oxygen evolution reaction. *Appl. Catal. B: Environ.* **2020**, *278*, 119295.

[45] Zhao, X. H.; Pattengale, B.; Fan, D. H.; Zou, Z. H.; Zhao, Y. Q.; Du, J.; Huang, J. E.; Xu, C. L. Mixed-node metal-organic frameworks as efficient electrocatalysts for oxygen evolution reaction. *ACS Energy Lett.* **2018**, *3*, 2520–2526.

[46] Qian, Q. Z.; Li, Y. P.; Liu, Y.; Yu, L.; Zhang, G. Q. Ambient fast synthesis and active sites deciphering of hierarchical foam-like trimetal-organic framework nanostructures as a platform for highly efficient oxygen evolution electrocatalysis. *Adv. Mater.* **2019**, *31*, 1901139.

[47] Zhao, K. Y.; Shen, Q. K.; Tao, Y.; Li, J. R.; Wang, M. L.; Li, C.; Xu, B. J. Atomically dispersed N/O-coordinated cobalt catalyst enables aerobic oxygenation of olefins under ambient conditions. *ACS Catal.* **2023**, *13*, 12591–12600.

[48] Li, Y.; Li, J. W.; Huang, J. H.; Chen, J. X.; Kong, Y.; Yang, B.; Li, Z. J.; Lei, L. C.; Chai, G. L.; Wen, Z. H. et al. Boosting electroreduction kinetics of nitrogen to ammonia via tuning electron distribution of single-atomic iron sites. *Angew. Chem., Int. Ed.* **2021**, *60*, 9078–9085.

[49] Ren, J. Y.; Li, Z.; Qu, B. H.; Meng, L. Y.; Bai, L. L.; Sun, J. H.; Zhang, Z. Q.; Qu, Y.; Jing, L. Q. Visual eosin Y-based photosensitization sensing systems for ultrasensitive detection of diclofenac with single-atom Co–N_2O_2 site-immobilized g-C_3N_4 nanosheets. *Adv. Mater.* **2024**, *36*, 2404392.

[50] Shi, J. J.; Wei, Y.; Zhou, D.; Zhang, L. L.; Yang, X. F.; Miao, Z. L.; Qi, H. F.; Zhang, S. X.; Li, A. Q.; Liu, X. Y. et al. Introducing Co–O moiety to Co–N–C single-atom catalyst for ethylbenzene dehydrogenation. *ACS Catal.* **2022**, *12*, 7760–7772.

[51] Ni, B. X.; Shen, P.; Zhang, G. R.; Zhao, J. J.; Ding, H. H.; Ye, Y. F.; Yue, Z. Y.; Yang, H.; Wei, H.; Jiang, K. Second-shell N dopants regulate acidic O_2 reduction pathways on isolated Pt sites. *J. Am. Chem. Soc.* **2024**, *146*, 11181–11192.

[52] Jiang, K.; Zhao, J. J.; Wang, H. T. Catalyst design for electrochemical oxygen reduction toward hydrogen peroxide. *Adv. Funct. Mater.* **2020**, *30*, 2003321.

[53] Han, J. X.; Tan, H.; Guo, K.; Lv, H. Y.; Peng, X. Y.; Zhang, W.; Lin, H. P.; Apfel, U. P.; Cao, R. The "pull effect" of a hanging Zn^{II} on improving the four-electron oxygen reduction selectivity with Co porphyrin. *Angew. Chem., Int. Ed.* **2024**, *63*, e202409793.

This is an open access article under the terms of the Creative Commons Attribution 4.0 International License (CC BY 4.0, https://creativecommons.org/licenses/by/4.0/).

© The Author(s) 2025. Published by Tsinghua University Press.